ACOUSTIC VALIDATION OF A NEW CODE USING PARTICLE WAKE AERODYNAMICS AND GEOMETRICALLY-EXACT BEAM STRUCTURAL DYNAMICS

Daniel G. Opoku[1] and Fred Nitzsche[2]
Department of Mechanical and Aerospace Engineering
Carleton University
Ottawa, Canada, K1S 5B6

Abstract

This paper describes the validation of a new code for predicting both aeroacoustic and aeroelastic behaviour of hingeless rotors. The structural component was based a non-linear beam element model considering small strains and finite rotations, which uses a mixed variational intrinsic formulation. The aerodynamic component was built on a low-order panel method incorporating a vortex particle free-wake model. The aerodynamic and structural components were combined to form a closely coupled aeroelastic code that solves in the time-domain. The loading and thickness noise terms for the aeroacoustic calculations were calculated from the aerodynamic data using a formulation based on the Ffowcs Williams-Hawkings (FW-H) equation. The code was successfully validated for acoustic signature and BVI predictions using test cases from the HELINOISE program.

Introduction

The objective of the current paper is to describe the development and initial validation of a new aeroelastic / aeroacoustic code to study noise and vibration in rotorcraft. The code interfaces separate aerodynamic and structural dynamic components. The aerodynamic component is based on a high-resolution unsteady panel method with a vortex particle model description of the free-wake. The structural component is a non-linear beam finite-element model of the rotor blades based on a mixed variational intrinsic formulation. Together, these components form a closely coupled aeroelastic code that is solved in the time domain. Data from the aerodynamic component is used to obtain acoustic results.

The development of this new code was the result of a collaboration involving the National Technical University of Athens (NTUA) in Greece, the Massachusetts Institute of Technology (MIT) in the USA and Carleton University in Canada. The referred partners provided the aerodynamic, structural and acoustic components, respectively. Through collaboration with NTUA, an existing aerodynamic code – GENeral Unsteady Vortex Particle or, shortly, GENUVP (Ref. 1) was modified within the current work to become the aerodynamic component of the new code. GENUVP has several powerful features, including the accurate modelling of wake effects, the ability to model various flight scenarios and full rotorcraft configurations The structural component of this work is based on a slightly modified version of a code originally developed at MIT (Ref. 2), which is based on a non-linear, “geometrically exact,” beam element representation of the rotorblades using the mixed variational intrinsic formulation first introduced by Hodges (Ref. 3). An aeroelastic interface was developed in a close cooperation involving Carleton University and the MIT to couple the aerodynamic and structural components in the time-domain (Fig. 1). The aeroacoustic component was developed at Carleton University (Ref. 4), based on the Ffowcs Williams-Hawkings (FW-H) equation (Ref. 5). The lifting surfaces of the blades were discretized into panel elements, each of which representing an elementary acoustic source. The total acoustic field produced by all panels was calculated based on the noise spectrum generated by replicating the aeroacoustic data retrieved after a periodic solution in the time-domain was achieved. To validate the aeroacoustic component of the new code, the HELINOISE experiment was used as the benchmark. The numerical results obtained with the code, including both the aerodynamic loading and acoustic signature of the rotorblades successfully validated the new code against test cases from the HELINOISE program.

Problem Formulation

Computational modelling of rotorcraft aeroacoustics is a unique and challenging problem. To properly model a rotorcraft, the non-linear aeroelastic interaction between several independently moving elastic bodies – the rotorblades must be captured. In addition, the influence of the free wake must be considered as it is of fundamental importance to predict the unsteady aerodynamic loads acting on the blades, and capture phenomena such as blade-

[1] Research Assistant. Presently, Research Engineer, United Technologies Research Center, USA.
[2] Professor. Email: fred_nitzsche@carleton.ca

vortex interaction (BVI) effects. These factors combined make aeroelasticity and, subsequently, aeroacoustics of rotorcraft a computationally very expensive task.

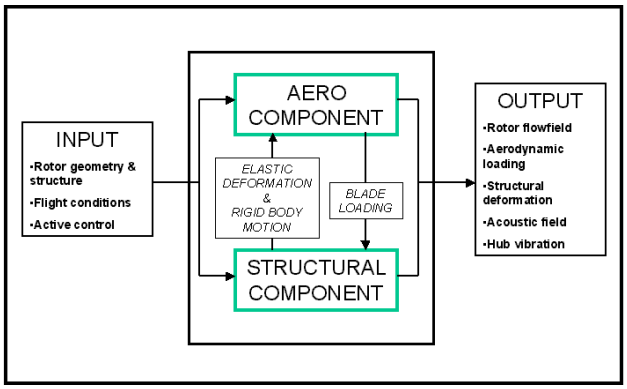

Figure 1: Basic composition of the code.

Aerodynamic Component

Grid-based Computational Fluids Dynamics (CFD) codes have been used with relative success to model rotorcraft aerodynamics (Refs. 6-7). While grid-based CFD has the potential to eventually provide detailed rotorcraft aerodynamic calculations, its use is currently limited because is too computationally expensive. Due to the presence of multiple independently moving elastic bodies and a relatively large flow domain, the generation of a suitable grid for rotorcraft is laborious. In addition, grid-based CFD has the difficulty of correctly capturing essential wake effects due to numerical dissipation. An alternative approach is to use a panel method or lifting-line model, coupled with a vortex wake model for aerodynamic modelling (Refs. 8-9). Although they provide lower resolution of the flow-field than the grid-based CFD, these methods can provide an accurate prediction of the aerodynamic loading on the rotor blades in a variety of flight situations. More importantly, the prediction is obtained with computational costs that are orders of magnitude less than grid-based CFD. GENUVP is an example of such a code, based on the panel method with a vortex particle wake model for calculating the flow-field around multi-component configurations. It was first developed for wind-turbine applications (Ref. 10). The basis of GENUVP is the Helmholtz decomposition principle. Using Helmholtz Principle, the flow-field around a rotorcraft can be decomposed into an irrotational part due to the presence of multiple bodies, and a rotational part due to the wakes emitted by lifting bodies. If $\vec{u}(\vec{x},t)$, $\vec{x} \in D$, $t \geq 0$ denotes the velocity around a rotorcraft as a function of the position, $\vec{x}$ and time, t and D is the flow-field domain:

$$\vec{u}(\vec{x},t) = \vec{u}_{ext}(\vec{x},t) + \vec{u}_{solid}(\vec{x},t) + \vec{u}_{near-wake}(\vec{x},t) + \vec{u}_{far-wake}(\vec{x},t) \quad (1)$$

In equation (1), $\vec{u}_{ext}$, $\vec{u}_{solid}$, $\vec{u}_{near-wake}$ and $\vec{u}_{far-wake}$ are, respectively, the specified external velocity for the given flight condition, the velocity due to the influence of solid bodies such as rotorblades, fuselage, and stabilizers, the velocity due to the influence of the near-wake and the velocity due to the far-wake. Using a panel method approach, $\vec{u}_{solid}$ and $\vec{u}_{near-wake}$ are given in terms of singularity distributions over the surface of the solid bodies extended to a "near wake," defined as shown in Figure 2. Next, Biot-Savart law provides means for obtaining $\vec{u}_{far-wake}$ due to a singularity situated at $\vec{x}_0$:

$$\vec{u}_{far-wake}(\vec{x},t) = \int_{D(t)} \frac{\vec{\omega}(\vec{x}_0,t) \times (\vec{x} - \vec{x}_0)}{4\pi \left| \vec{x} - \vec{x}_0 \right|^3} dD \quad (2)$$

In equation (2) $\vec{\omega}$ is the vorticity vector associated with the singularity.

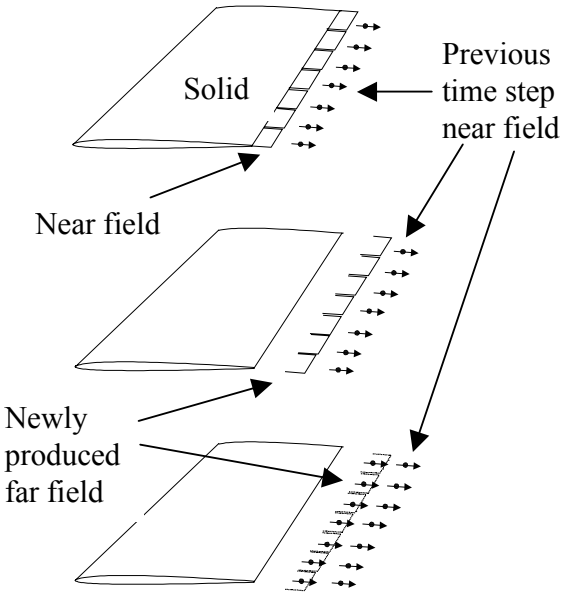

Figure 2: The formation of vortex particles from a trailing edge wake strip.

Following the panel method calculations at a given time step, the "near-wake" strip elements are transformed into vortex particles and become part of the "far-wake." Integrating the vorticity of each near-wake dipole element produces a vortex particle. The new vortex particles become part of the far wake,

which evolves prior to the next time step using a Lagrangean description of the flow. Figure 2 gives a schematic of the so-called "vortex blobs" formation process. Details of the aerodynamic model can be found in other publications (Refs. 1, 4).

Rigid Blade Results. Figure 3 shows a visualization of the wake produced by a typical rotor in forward flight, at an advance ratio of 0.14 using GENUVP. The formation and expansion of tip vortices at the edges of the rotor disc are visible.

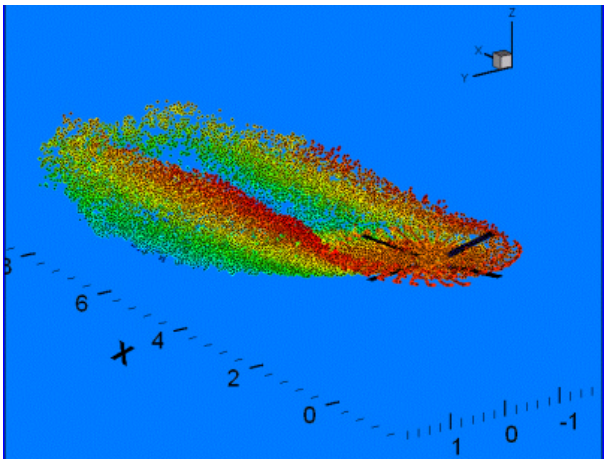

Figure 3: Visualization of the free wake produced by a typical four-bladed rotor in forward flight (Ref. 4).

Figure 4 shows a comparison of the final solution for blade spanwise loading. The comparison results were from a CAMRADII simulation, run as part of the analysis done by Shin (Ref. 11). The two codes predicted a similar spanwise load distribution, which increased with radial distance. Both codes predicted a peak in the spanwise loading between the stations 90% and 100% of the radius. The codes differed in the magnitude of the predicted peak. This difference can be attributed solely to the difference in the wake geometry between the two models – specifically, the difference in the amount of wake contraction. It should be noted that the amount of wake contraction in CAMRAD II is based on a specified parameter calculated from the measured wake geometry (Ref. 12), which was not available from the experiment in the present case.

Figure 5 shows a comparison of the total lift loading for a single blade over a period of two complete rotor revolutions. Likewise in the previous case, the comparison was against results obtained by Shin (Ref. 11) using Peter and He's finite-state induced flow model (Ref. 13).

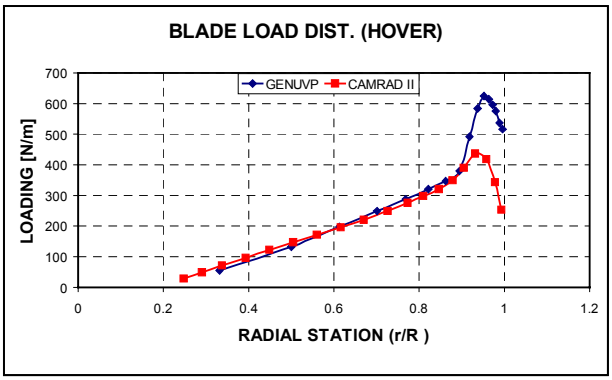

Figure 4: Blade spanwise loading of a typical blade in hover (Ref. 4).

For the latter result, both codes compared favourably in terms of overall trends. Differences could mainly be attributed to the difference in the wake modelling, which allowed GENUVP to capture higher frequency loading variations than the finite-state induced flow model.

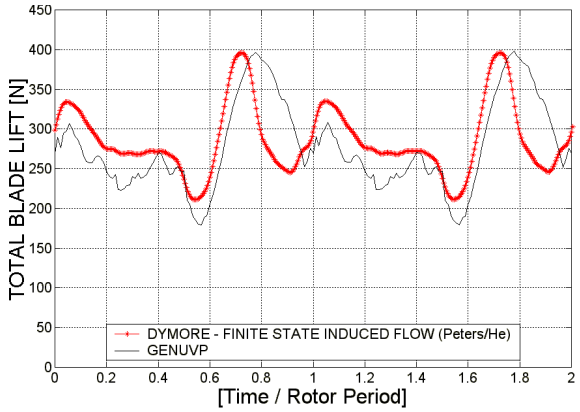

Figure 5: Total lift loading on a single blade in forward flight (Ref. 4).

Structural Component

Hodges developed a mixed variational approach to develop a "geometrically exact" formulation for the dynamics of rotating beams (Ref. 3). Hodges' formulation decomposes the analysis of the three-dimensional blade structure into a linear analysis of the cross-section geometry and material properties, and a non-linear one-dimensional analysis along the beam reference line. A geometrically exact description of the beam reference line makes Hodges' formulation suitable for capturing the large deformations that rotor blades typically experience. In addition, Hodges' formulation uses full constitutive

relations for elastic and inertial properties, allowing capture of the coupling between the beam degrees of freedom. Shang extended the work of Hodges by writing the mixed variational equations of motion in a global rotating frame, and applying the finite element method for spatial discretization (Ref. 14). In the latter formulation, three coordinate frames were used in the equations of motion: global "*a*", local non-deformed "*b*", and local deformed "*B*". A diagram of the coordinate frames is shown in Figure 6. Frame "*a*" is a global rotating frame, which follows the blade around the rotor azimuth angle. Frame "*b*" describes the local non-deformed orientation of the blade reference line as a function of a spanwise curvilinear coordinate. The latter frame accounts only for the initial curvature and pre-twist of the blade, and it can be related to frame "*a*" through direction cosine transformations. Frame "*B*" describes the locally deformed orientation of the beam reference line. This frame includes both rigid and elastic rotations due to arbitrarily large angles. The use of these three reference frames allows a compact, "geometrically exact" beam formulation, while also allowing the use of constitutive relations solely based on the deformed reference frame "*B*." Further details of this analysis are found in the original work by Shang (Ref. 14).

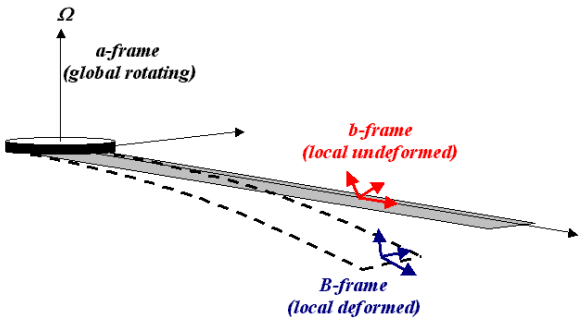

Figure 6: A schematic diagram of the coordinate frames used by the structural component.

Adopting the finite element method, the spatial domain of the blade is discretized into *N* spanwise elements. Once the discretization is applied, a set of non-linear partial differential equations in time can be written. In matrix notation:

$$F_S(X,\dot{X}) - F_L = 0 \qquad (3)$$

where F_S is the structural operator, F_L is the load operator, and X is the unknown vector consisting of structural variables: discrete measures of displacement, rotation, internal loads, moments, and selected boundary values. It is worthwhile to stress that in this formulation the form of X depends on the type of rotor boundary conditions being considered. For example, for the hingeless rotor tested in the HELINOISE program, the unknown boundary quantities included in X are the blade root forces and moments and the blade tip displacements and rotations.

Equation (3) gives a geometrically exact description of the dynamics of a rotating beam. To apply a numeric method to solve these equations, two main considerations are necessary; namely, a method for computing the derivatives and a scheme for solution of the non-linear equations of motion. When selecting numeric methods for the non-linear system solution, the accuracy, stability, and computational cost issues were considered. Stability was an especially important consideration to avoid introduction of numerical oscillations and instabilities into the solution. Cheng developed at the MIT a structural code based on Shang's formulation (Ref. 2). The structural code solves the non-linear equations of motion in a time-marching fashion. An Euler, second-order backward finite difference scheme, was applied to numerically approximate the derivatives in (3) and solve iteratively for the X vector of unknowns. Further details of the method and the validations associated with the structural component are found in a previous work (Ref. 15).

Aeroelastic Coupling

The two separate representations of the rotor (i.e. the aerodynamic and structural components) were formulated and solved independently. At each time step, aeroelastic data (loads, aerodynamic damping, deformation, and deformation rates) were exchanged between the two components as shown in Figure 1. This process is repeated until a periodic solution is found in the time domain.

The aeroelastic coupling between the aerodynamic and structural components was based on an extension of the simple aeroelastic problem of a two-dimensional airfoil section, depicted in Figure 7. In the Figure, the airfoil section is shown with degrees of freedom in the plunge (vertical), lag (horizontal), and pitch (rotational) degrees of freedom. These degrees of freedom are elastically restrained, represented in the Figure by linear and torsional springs at the beam reference point. Offsets between both the beam reference axis and aerodynamic centre, $\bar{X}_{CG}$ and centre of gravity, $\bar{X}_a$ were considered. This system was extended to three dimensions in the following manner. At every spanwise section, loading is computed by the aerodynamic component, including the effect of

elastic velocity and torsional rotation about the beam reference axis. Although the structural component has six degrees of freedom at each spanwise node, only three displacements and one rotation, namely, the plunge (flap), lag, extension, and pitch degrees of freedom were considered for the aeroelastic coupling.

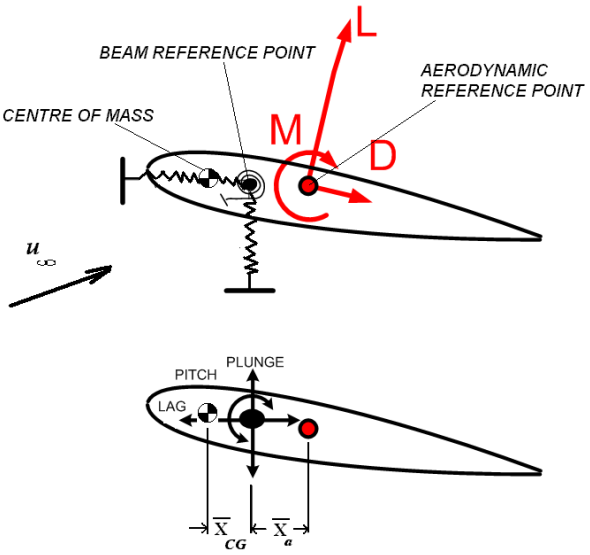

Figure 7: Schematic diagram of the basis for aeroelastic coupling of the aerodynamic and structural components.

By extending the two-dimensional aeroelastic system to three dimensions, a framework is developed for coupling the aerodynamic and structural components, as shown schematically in Figure 8.

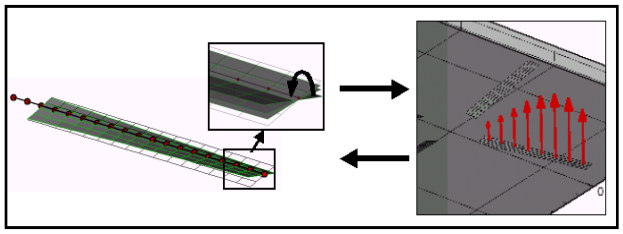

Figure 8: Schematic diagram of the code aeroelastic coupling method

The structural and aerodynamic components retained in the code separate representations of the blade. The structural component used a one-dimensional beam element discretization of the beam reference axis to model the blade structure, typically from the hub attachment point to the blade tip. The aerodynamic component modelled the three-dimensional lifting surface of the blade as a two-dimensional surface consisting of panel elements. Each section of the three dimensional lifting surface was similar to the problem shown in Figure 7. The effective section loading and elasticity were provided by the aerodynamic and structural components, respectively. The aerodynamic component solved for the potential loading L at every spanwise station. Using L, the effective section angle of attack was calculated. Next, using airfoil lookup tables, the section drag D was obtained to correct for the viscous effects, which cannot be captured by the potential theory. The pitching moment coefficient was also obtained from the airfoil lookup tables to avoid the need for a very fine discretization near the airfoil leading edge, hence further decreasing the computational costs. The airfoil tables were typically indexed by both angle of attack and section Mach number, allowing for compressibility corrections. The spanwise loading distribution was applied by the structural component to the beam reference axis to solve for the aeroelastic response. The elastic deformation of the blade was then used to deform the aerodynamic mesh of the lifting surface, as depicted in Figure 8. The rate of elastic deformation of the blade provided an additional body velocity component that was accounted for in the non-penetration condition in the aerodynamic formulation.

Aeroacoustic Component

Ffowcs-Williams and Hawkings derived the FW-H equation based on the Lighthill acoustic analogy (Ref. 5). The FW-H equation treats the problem of sound generated by a body in arbitrary motion in a fluid as a problem of mass and momentum conservation, with a mathematical surface discontinuity corresponding to the body surface. Outside of the surface, the exterior flow field defines the domain; the flow on the interior of the surface is arbitrary (although, typically, assumed to be at rest). Mass and momentum sources are used to create the surface discontinuity, and ultimately act as sound generators. The acoustic analogy is then applied to obtain the governing equation of the problem.

The fluid mass and momentum conservation equations are written next, including the surface discontinuity, and combined to obtain a wave equation. Letting $\vec{x}$ and $\vec{y}$ be the observer and source position vectors, respectively, and $f(\vec{y},t)=0$ describe the motion of the surface of a body, the FW-H equation reads (Ref. 5):

$$\left(\frac{1}{c^2}\frac{\partial^2}{\partial t^2}-\nabla^2\right)p' = \frac{\partial}{\partial t}\left[\rho_o v_n |\nabla f|\delta(f)\right] - \frac{\partial}{\partial x_i}\left[l_i|\nabla f|\delta(f)\right] + \frac{\partial^2}{\partial x_i \partial x_j}\left[T_{ij}H(f)\right] \quad (4)$$

Equation (4) gives the sound generated by the body moving through a fluid, where p' is the acoustic pressure measured at the observer position, $\vec{x}$; c and ρ_0 are the speed of sound and the density of the undisturbed medium, respectively; v_n is the local normal velocity on the body surface, l_i is the local force on the fluid per unit area, and T_{ij} is the Lighthill stress tensor; $\delta(f)$ and $H(f)$ are the Dirac delta and Heaviside functions, respectively.

The three terms on the right-hand side of the equation are associated to the "thickness," "loading," and "quadrupole" noise sources, respectively. The thickness source accounts for noise due to the displacement of the fluid by the finite thickness of the body; the loading source accounts for noise due to loading and changing of pressure loading on the body. The noise due to compressibility effects is included in the quadrupole source. The loading and thickness noise are surface sources, whereas the quadrupole noise is a volume source. In the current work, the quadrupole noise source could not be considered because it required a grid-based flow solver. However, neglecting the quadrupole term is a practical approximation as the thickness and loading noise terms, which account for the noise when the flow is not transonic (Ref. 16). Thus, the present formulation is valuable for a great deal of rotor noise prediction applications, including BVI, which is mostly generated at lower advance ratios.

In the current work, an acoustic formulation based on Farassat's 1A solution of the FW-H equation (Ref. 17) was pursued. The 1A formulation is a solution of the FW-H equation for thickness and loading noise sources obtained by integration on the body surface. The 1A formulation is a well-validated method that is used extensively in rotorcraft aeroacoustics (Refs. 18, 19). There are enhancements for approximating the quadrupole term, but those were not considered in the present work (Ref. 20).

The complete derivation of the 1A formulation can be found in the original work by Farassat and Succi (Ref. 17). Therefore, only the final solution is repeated next:

$$4\pi p'_L(\vec{x},t) = \frac{1}{c}\int_{f=0}\left[\frac{l_i r_i}{r(1-M_r)^2}\right]_{ret} dS + \int_{f=0}\left[\frac{l_r - l_i M_i}{r^2(1-M_r)^2}\right]_{ret} dS + \frac{1}{c}\int_{f=0}\left[\frac{l_r\left(rM_i r_i + cM_r - cM^2\right)}{r^2(1-M_r)^3}\right] dS \quad (5)$$

$$4\pi p'_T(\vec{x},t) = \int_{f=0}\left[\frac{\rho_0 v_n\left(rM_i r_i + cM_r - cM^2\right)}{r^2(1-M_r)^3}\right]_{ret} dS \quad (6)$$

where $\vec{r} = \vec{x} - \vec{y}$, $M_i = v_i/c$ is the local Mach number, $M_r = M_i\, r_i/r$ is the radial Mach number and $l_r = l_i\, r_i/r$. Equations (5) and (6) produce the loading and thickness pressure contributions to the total acoustic pressure, $p'(\vec{x},t) = p'_L(\vec{x},t) + p'_T(\vec{x},t)$ measured at the observer position, $\vec{x}$. The subscript *ret* indicates that the integrals must be evaluated in the "retarded" time frame τ, defined by the time at which the acoustic signal was emitted. The acoustic signal history is measured at the observer position, in the observer time frame, t. In the present solution, the integrals shown in equations (5) and (6) were numerically evaluated by discretizing the body surface into elements and adding up the elementary contributions to the two acoustic components. The acoustic component of the developed code used the same discretization as the aerodynamic component, treating each panel as an acoustic source. After the potential calculations were completed, the aerodynamic results were used to calculate the emitted acoustic signals. At the end of the simulation, the predicted acoustic pressure history at each specified microphone (observer position) was obtained. The loading noise contribution of each panel was calculated as a function of the potential loading, velocity, and distance to the microphone. Viscous corrections were not included. Special consideration was needed for the thickness noise term since thin lifting bodies were used in the current work, and the thickness noise term is dependant on v_n the local normal velocity on the actual blade surface. Therefore, for each actual panel, projected upper and lower surface "virtual" panels were determined from the known airfoil geometry. The normal velocity was then calculated for the upper and lower surface panels using the velocity of the mean surface panel, and the normal vectors of the projected panels (Figure 10). The thickness noise

contribution was then evaluated as the sum of the contribution of the upper and lower projected panels.

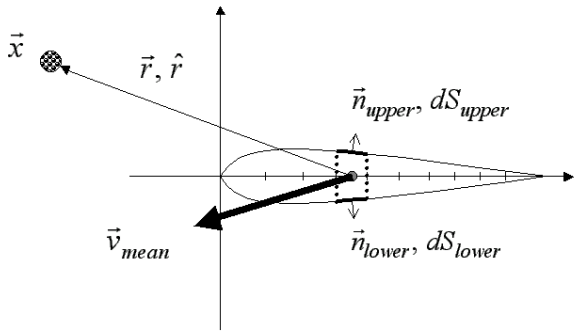

Figure 10: Illustration of the method used to calculate the normal velocity on the actual blade surface.

Once the acoustic pressure contribution of each panel was calculated, the total acoustic pressure history at each microphone could be determined by summation, taking into account time sequencing due to the difference in travel distance for each acoustic emission. Considering Figure 11, an approximation for the relation between the source time (when the signal is emitted) and the observer time (when the signal is received) was obtained for the acoustic signal $p'(\vec{x},\tau_i)^k$ emitted by the k^{th} panel at time τ_i in the source time frame, which was identified to the time frame at which the aerodynamic calculations were computed ($\hat{r}$ is the unit vector in the direction of $\vec{r}$ and $\vec{u}_\infty$ is the undisturbed flow velocity vector):

$$t = \tau + \frac{|\vec{r}|}{c + \vec{u}_\infty \cdot \hat{r}} \qquad (7)$$

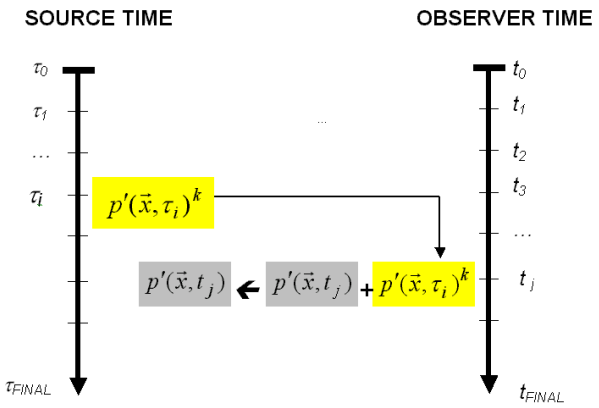

Figure 11: Diagram of the time-shifting scheme used to determine the acoustic pressure history in the observer time scale.

Rigid Blade Results. For the purpose of validation of the acoustic component alone, the scaled model of the two-bladed teetering UH1H rotor was used. Details of the scaled UH1H rotor are found in the open literature (Ref. 21). To accurately capture the acoustic signal, very fine discretization is required in both space and time. By running repeated test cases, it was found that the time step size to accurately capture the acoustic signal was 90 time steps per revolution. In comparison, a resolution of 60 time steps per revolution was sufficient for accurate aerodynamic results. It was also found that a fine chordwise discretization of the blade, with further refinement at the leading edge, was required for producing accurate results. Figures 12a-c depict comparisons of the loading, thickness, and total acoustic pressures, respectively, measured at a microphone situated 3 m from the hub, in the plane of the rotor, in hover. Comparison results are from the original version of the commercial code WOPWOP (Ref. 22), which uses a slightly modified Farassat 1A acoustic formulation. The two codes agree well in all three comparisons. The slight time shift visible in the results is caused by the difference, between the two codes, of the starting position of the rotor.

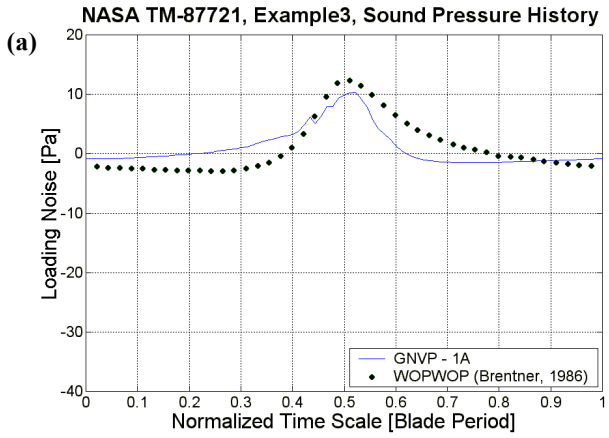

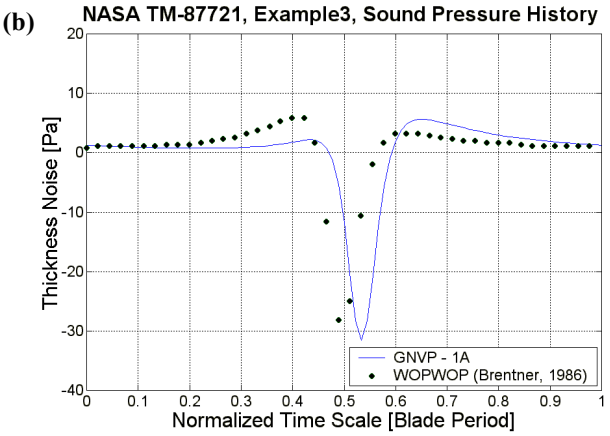

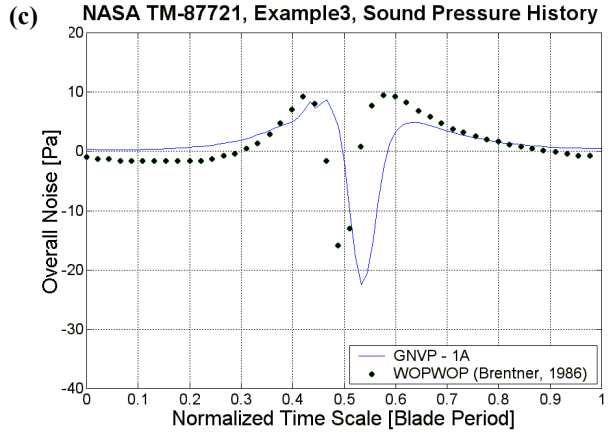

Figure 12: Comparisons of acoustic pressures for the UH1H rotor in hover: (a) Loading; (b) Thickness; (c) Total.

Figure 13 shows a visualization using the present code, of the wake produced by the UH1H rotor in forward flight (0.208 advance ratio and 8.85° forward disc tilt angle) and the locations of two microphones where acoustic pressure was compared. Microphone 4 was situated 4 m ahead of the rotor hub on the advancing side and microphone 5 4 m ahead of the rotor hub on the retreating side.

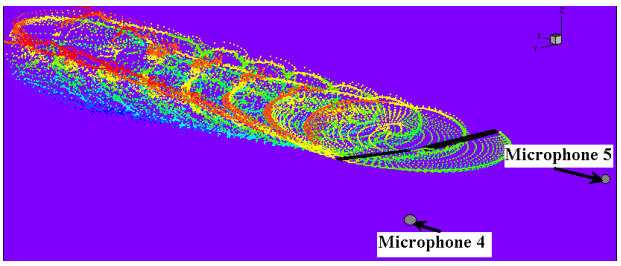

Figure 13: Visualization of the wake produced by the UH1H rotor in forward flight and the locations of the microphones.

Figures 14a-b show a comparison of the total acoustic pressures at the two microphone locations. Comparisons are given with both experimental (Ref. 21) and WOPWOP data (Ref. 22) for the advancing side microphone, and with experimental data alone for the retreating side microphone. In both cases, the overall trend was captured by the present code. The higher frequency component present in the experimental results was not captured by either code. While some of this high frequency component may be due to experimental scatter, it is suspected that the oscillations may be due to blade flexibility effects. Ffowcs-Williams and Hawkings stated that the only restriction placed upon a surface in the FW-H equation is that it should be smooth; otherwise it would be allowed to move in an arbitrary fashion and change its shape or orientation (Ref. 5).

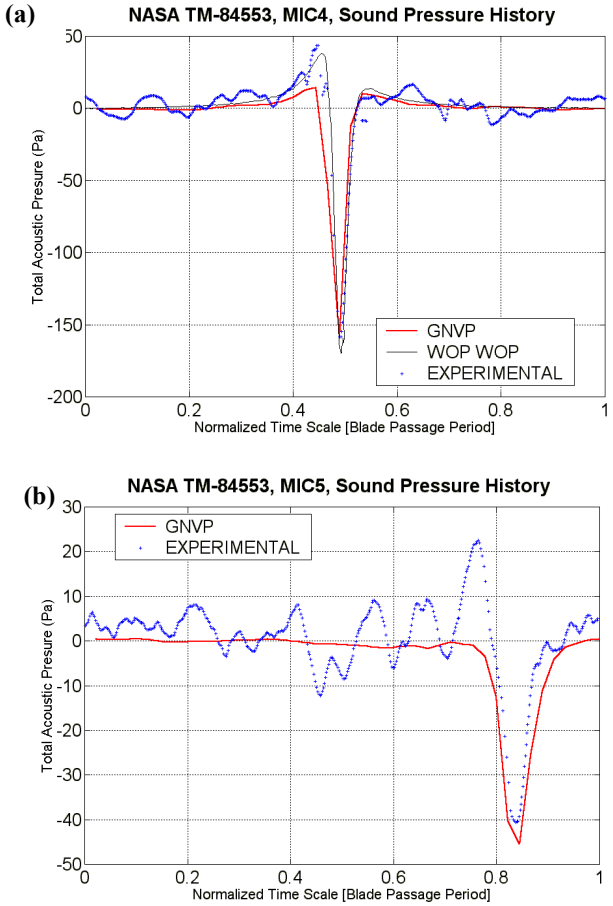

Figure 14: Comparison of total acoustic pressure for the UH1H in forward flight: (a) Advancing side microphone; (b) Retreating side microphone.

Figure 15 depicts a comparison of sound pressure level, SPL ($SPL = 20\log\left(p'/p_{ref}\right)$, p_{ref} = 20 μPa) versus frequency for the microphone on the advancing side of the rotor against the experiment results (Ref. 21). The peaks in SPL at harmonics of the blade passage frequency were accurately captured by the present code. The overall trend of the frequency spectrum was captured as well.

Code Results and Validation

In the HELINOISE program, a scaled model of the main rotor of an ECD BO105 four-bladed hingeless helicopter was constructed (Ref. 23). A summary of rotor data for the BO105 model is presented in Table 1. The test rotor was scaled forty-percent

geometrically, in addition to Mach number and dynamic scaling. One of the test rotor blades was extensively instrumented with pressure transducers to measure aerodynamic loads, and with strain gauges to measure the blade flapping, lead-lagging, and torsional deformation. The HELINOISE test was conducted in the German-Dutch Wind Tunnel (Ref. 24),

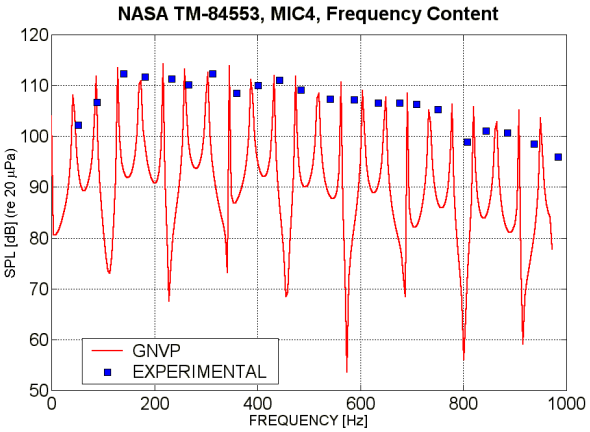

Figure 15: Comparison of frequency content of the total acoustic pressure prediction of the advancing side microphone for UH1H in forward flight.

A transversing microphone array was used during the experiment to measure the rotor acoustic signature on a plane below the rotor. The HELINOISE test plan included hover, level flight, climb and descent conditions, over a range of advance ratios. Particular attention was paid to descent flight conditions to capture BVI event test data.

Table 1: Data summary for the BO105 model rotor.

Scaling factor	2.455
Number of blades	4
Rotor type	Hingeless
Airfoil	NACA 23012 modified
Rotor radius	2 m
Blade chord	0.121 m
Pre-twist (outboard of r = 0.44 m)	-4° /m
Nominal rotor speed, Ω	1050 RPM (110 rad/s)

Although effort was made to model the HELINOISE test set-up in the present validations as closely as possible, certain approximations were necessary due to lack of availability of detailed blade structural data and for simplification purposes. Only the lifting surfaces of the blades are modelled with both the structural and aerodynamic components, with a cantilevered root boundary condition for the blade flapping and lead-lagging motion. This simplification means that the present numerical model does not include the effects of flexibility of the blade root cutout. The fuselage present in the tests was not considered in the present model, which would have some effect on the aerodynamic results due to changes in the inflow, and on the acoustic results due to acoustic shielding of microphones. Finally, due to lack of availability of detailed blade construction information, some of the structural input data were estimated by comparison with similar aeroelastically scaled model rotors. Table 2 gives a summary of the blade section inertial and elastic properties used for structural input in the code. An asterisk denotes properties that are estimated using indirect data.

Table 2: Summary of inertial and elastic properties used in the present work.

m	0.948 kg/m
I_{11}	6.23×10^{-4} kg-m^2/m
I_{22}*	8.89×10^{-6} kg-m^2/m
I_{33}*	6.10×10^{-4} kg-m^2/m
EA*	1.64×10^{6} N
GJ	2.50×10^{2} N-m^2
EI_{FLAP}	1.90×10^{2} N-m^2
EI_{LAG}	4.71×10^{3} N-m^2

*Parameter estimated by comparison with similar aeroelastically scaled rotors.
NOTE: The beam reference axis at 21% chord.

The present paper includes the predictions for the HELINOISE test case 1333 (Low-speed descent (0.15 advance ratio, -6° flight path angle). Results for additional test cases can be found in another work (Ref. 4). The test case demanded a total simulation length of approximately eighteen rotor revolutions. Over the first three revolutions, the loads transferred to the structural component were linearly increased to minimize structural transient oscillation due to the impulsive starting of the rotor. To allow this initial structural transient response to decay, ten revolutions were then used from the time of full load application to the start of particle wake activation. The particle wake was activated during the final five revolutions. The results became periodic prior to the final three revolutions. A typical run took about 48 hours in a single processor desktop personal computer equipped with a 2GHz clock.

Aerodynamic Loading

The normal force coefficient was measured on a radial section of the blade, normal to the section chord. The normal force coefficient can be used to

detect blade-vortex interaction (BVI) encounters. Theoretically, BVI is expected in the first and last quadrant of the azimuth cycle. Figure 16a shows the predicted normal force coefficient history at the outer portion of the blade, for one revolution, for HELINOISE case 1333; Figure 15b shows the experimental results for the same case. The present code accurately predicted the overall trend and magnitude of the normal force coefficient history. In addition, the BVI events on the advancing and retreating sides were captured. The magnitude of the predicted BVI on the retreating side was larger than the experimental measurement.

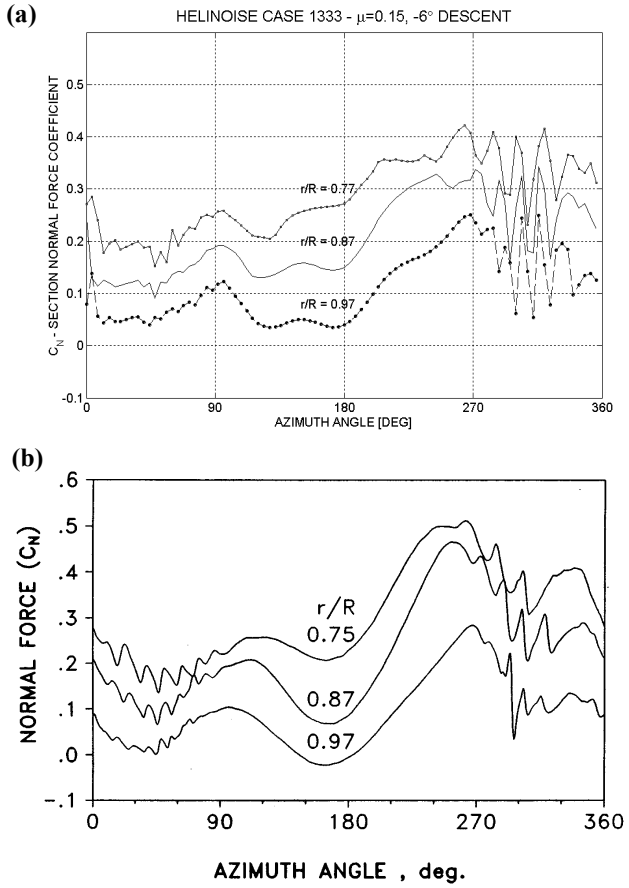

Figure 16: Normal force coefficient for HELINOISE case 1333: (a) Predicted. (b) Experimental (Ref. 24).

Acoustic Results

During the HELINOISE experiment, the acoustic signals were measured on plane approximately 1.2 rotor radii below the rotor hub, as shown in Figure 17. Collecting data on such a grid allows a comprehensive evaluation of the intensity and directivity of noise produced by the rotor. An acoustic grid that matches the points that were used in the HELINOISE experiment was specified for the present model for test case 1333.

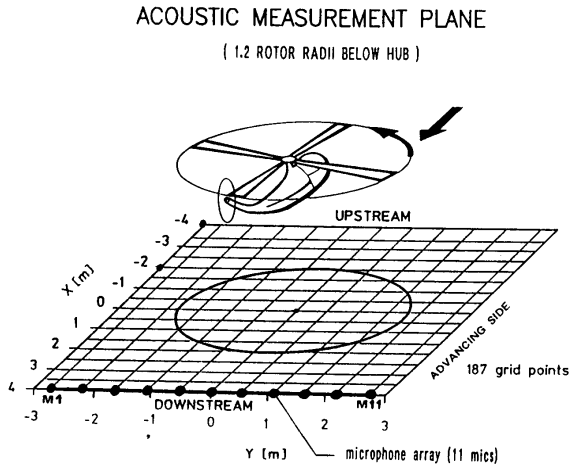

Figure 17: HELINOISE acoustic measurement plane relative to the model rotor. Microphone positions (Ref. 24).

The HELINOISE experimental acoustic measurements were reduced to a single acoustic measurement index called the frequency summary level or FSL for each microphone location (Ref. 23). Using a Fast Fourier Transform, data were converted into a narrowband frequency versus magnitude spectrum. The magnitude was expressed on a decibel scale. This spectrum had distinct tones at harmonics of the blade passage frequency. Frequency summary levels were obtained by adding the sound pressure levels of harmonics within a selected frequency range. The low-frequency summary level (LFSL) included harmonics up to the 10^{th} of the blade passage frequency, and was an index of the impulsive noise. By computing frequency summary level data on a grid such as that used in the HELINOISE experiment, contour plots could be produced in the present work giving an indication of noise intensity and directivity capabilities. The predicted LFSL value was calculated for each microphone and the summation taken up to the tenth harmonic:

$$LFSL = 10\log\left(\sum_{i=1}^{10} 10^{SPL_i/10}\right) \qquad (7)$$

Figure 18a shows the LFSL contour plot for HELINOISE case 1333, produced using acoustic pressure result predictions from the present code. A projection of the rotor circumference is shown with a black circle. Figure 18b is the LFSL plot for the same case, produced with measured results. The code predictions displayed similar directivity and intensity

trends as the measured results. The numerical results predicted a similar intensity range over the extent of the comparison range, but were slightly higher. The region of high noise intensity was correctly predicted downstream of the hub, within the projected rotor area. An intensity gradient was visible just upstream of the rotor hub, slanted in the cross flow direction. The predicted gradient was more slanted than the measured gradient. Differently from the measured results, peaks were predicted on the retreating side, downstream the hub. These peaks were consistent with the over-prediction of BVI intensity on the retreating side, discussed before. Although the predicted LFSL plot was respectable, results can be improved by decreasing the simulation time step size, in order to capture the acoustic signals with better resolution.

Conclusions

A new code to predict the aeroelastic and aeroacoustic behaviour of helicopter rotors was developed. The acoustic component was designed for predicting the thickness and loading acoustic pressure histories, for rotors in hover and forward flight. The acoustic component predictions were validated by comparison with computational and experiment data available from the HELINOISE experiment, both in the time and frequency domain. The aeroacoustic predictions produced magnitudes and trends that were similar to the experimental results. A respectable capability for prediction of the rotor acoustic signature and blade aerodynamic loading of a rotorcraft was demonstrated in the paper.

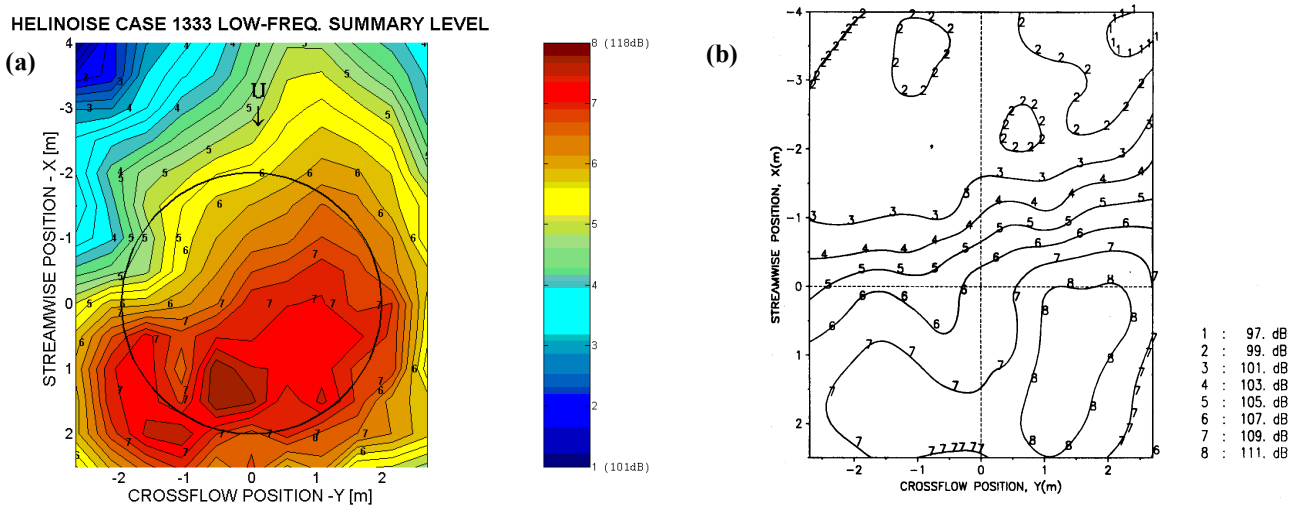

Figure 18: Low-frequency summary level plots (up to the 10th harmonic) for HELINOISE case 1333: (a) Code predictions. (b) Experimental (Ref. 24).

References:

1. Voutsinas, S. G., 1990, "A GENeralized Unsteady Vortex Particle Method (GENUVP) for Solving the Unsteady Flow around Multi-component Configurations," Report, Dept. of Mechanical Engineering, Fluids Section, National Technical University of Athens, Greece.
2. Cheng, T., 2002, "Structural dynamics modeling of helicopter blades for computational aeroelasticity," Master's of Science Dissertation, Massachusetts Institute of Technology, Cambridge, MA, USA.
3. Hodges, D. H., 1990, "A Mixed Variational Formulation based on Exact Intrinsic Equations for Dynamics of Moving Beams", *Int'l Journal of Solids and Structures*, vol. 26, no. 11, pp. 1253-1273.
4. Opoku, D. G., 2002, "Aeroelastic and Aeroacoustic Modelling of Rotorcraft," Master of Applied Science Dissertation, Dept. of Mechanical and Aerospace Engineering, Carleton University, Ottawa, Canada.
5. Ffowcs-Williams J. E. and Hawkings, D. L., 1969, "Sound Generation by Turbulence and Surfaces in Arbitrary Motion", *Philosophical Transactions of the Royal Society,* A264.

6. Strawn, R. C. and Djomehri, R. C., 2001, "Computational Modelling of Hovering Rotor and Wake Aerodynamics", *Proc. 57th AHS Annual Forum*, Washington, DC, May 9-11, pp. 1723-1734.
7. Pahlke, K. and Chelli, E., 2000, "Calculation of Multibladed Rotors in Forward Flight using a 3D Navier-Stokes Method", *Proc. 26th European Rotorcraft Forum*, The Hague, Netherlands, Sept. 26-29.
8. Voutsinas, S. G. and Triantos, D. G., 1999, "High-resolution Aerodynamic Analysis of Full Helicopter Configurations", *Proc. 25th European Rotorcraft Forum*, Rome, Italy, Sept. 14-16.
9. Voutsinas, S. G. and Triantos, D. G., 1999, "Aeroacoustics of Full Helicopter Configurations using Vortex Particle Flow Approximations", *Proc. CEAS Forum on Aeroacoustics of Rotors and Propellers*, Rome, Italy, June 9-11.
10. Voutsinas, S. G., Belessis, M. A. and Rados, K. G., 1995, "Investigation of the Yawed Operation of Wind Turbines by means of a Vortex Particle Method", *Proc. FDP Symposium on Aerodynamics and Aeroacoustics of Rotorcraft (AGARD CP552)*, Berlin, Germany.
11. Shin, S., 2001, "Integral Twist Actuation of Helicopter Rotor Blades for Vibration Reduction," PhD dissertation, Dept. of Aeronautics and Astronautics, Massachusetts Institute of Technology, Cambridge, MA, USA.
12. W. Johnson, 1998, "Rotorcraft Aerodynamics Models for a Comprehensive Analysis", *Proc. American Helicopter Society 54th Annual Forum*, Washington, DC, May 20-22.
13. D.A. Peters and C.J. He, 1995, "Finite State Induced Flow Models Part II: Three-Dimensional Rotor Disk", *Journal of Aircraft*, Vol. 32, No. 2, pp 323-333.
14. Shang, X., 1995, "Aeroelastic Stability of Composite Hingeless Rotors with Finite-State Unsteady Aerodynamics," PhD dissertation, School of Aerospace Engineering, Georgia Institute of Technology, Atlanta, Georgia.
15. Opoku, D. G., Nitzsche, F., Chang, T. and Cesnik, C. S., 2002, "Aeroelastic Modeling of Active Twist Rotorblades Using Particle-Wake Aerodynamics and Non-Linear Beam Structural Dynamics," Paper IMECE 2002-32961, *Proc. 2002 ASME International Mechanical Engineering Congress and Exposition*, New Orleans, LA, USA, November 17-22.
16. Brentner, K. S., 2000, "Modeling Aerodynamically Generated Sound: Recent Advances in Rotor Noise Prediction", *Presented at 38th Aerospace Sciences Meeting and Exhibit*, AIAA 2000-0345, January 10-13, Reno, Nevada, USA.
17. Farassat, F. and Succi, G. P., 1983, "The Prediction of Helicopter Rotor Discrete Frequency Noise", *Vertica*, Vol. 7, No. 4, pp. 309-320.
18. Schultz, K. J. et. al., 1994, "Aeroacoustic Calculation of Helicopter Rotors at DLR", *Proc. AGARD FDP Symposium on Aerodynamics and Aeroacoustics of Rotorcraft*, *CP552*, Berlin, Germany, Oct. 10-13.
19. Beaumier et. al., 1994, "Effect of Higher Harmonic Control on Helicopter Rotor Blade-Vortex Interaction Noise: Prediction and Initial Validation", *Proc. AGARD FDP Symposium on Aerodynamics and Aeroacoustics of Rotorcraft*, *CP552*, Berlin, Germany, Oct. 10-13.
20. Brentner, K. S., 1997, "An Efficient and Robust Method for Predicting Helicopter High-Speed Impulsive Noise", *Journal of Sound and Vibration*, Vol. 23, No. 1, pp. 87-100.
21. Conner D. A. and Hoad, D. R., 1982, "Reduction of High-Speed Impulsive Noise by Blade Planform Modification of a Model Helicopter Rotor", TM-84553, NASA Langley Research Centre, Hampton, VA, USA.
22. Brentner, K. S., 1986, "Prediction of Helicopter Rotor Discrete Frequency Noise: A Computer Program Incorporating Realistic Blade Motions and Advanced Acoustic Formulation", TM-87721, NASA Langley Research Centre, Hampton, VA, USA.
23. Kloppel, V., 1995, "Helicopter and Tilt-Rotor Aircraft Exterior Noise Research (HELINOISE)", *Advances in Acoustics Technology*, John Wiley and Sons, New York, NY.
24. Splettstoesser, W. R. et. al., 1993, "The HELINOISE Aeroacoustic Rotor Test in the DNW – Test Documentation and Representative Results", DLR-Mitt. 93-09, DLR, Braunschweig, Germany.

Acknowledgements

The authors wish to thank their collaborators, in particular Prof. S. Voutsinas from the Technical University of Athens, in Greece, who was the original developer of the GENUVP aerodynamic code and Prof. C. Cesnik, presently at University of Michigan, Ann Arbour, USA, who supervised the development of the structural component used in the present code.

Appendix
Individual Microphone Results

Figure A1 shows the predicted acoustic signal with the transversing microphone array, 2 m downstream of the rotor hub for HELINOISE case 1333. Microphone 1 was on the retreating side, with the microphone numbers increasing to Microphone 11, which is on the advancing side. For comparison, the experimentally measured results are shown in Figure A2. Both results present a periodic signal that repeats four times per revolution, corresponding to the blade passage frequency. The predicted acoustic signals were similar to the measured acoustic signals in terms of waveform and magnitude. The similarity along the span of the microphone array indicates the capture, by the present code, of the directivity of the rotor noise. A primary difference between the numerical and measured results was that the impulsive pressure peaks, of the microphones on the retreating side, were not consistently predicted. This was likely due to a truncation error, which could be resolved by using a smaller time step size, to capture the impulsive nature of the acoustic signal.

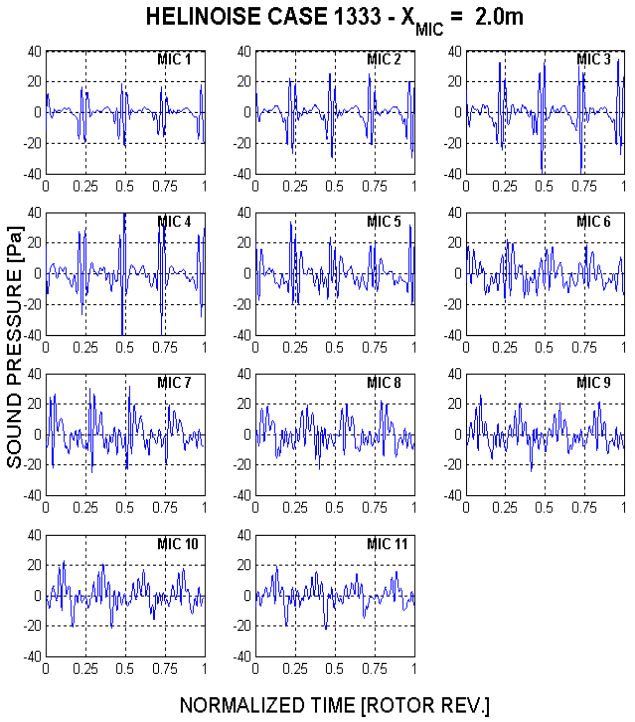

Figure A1

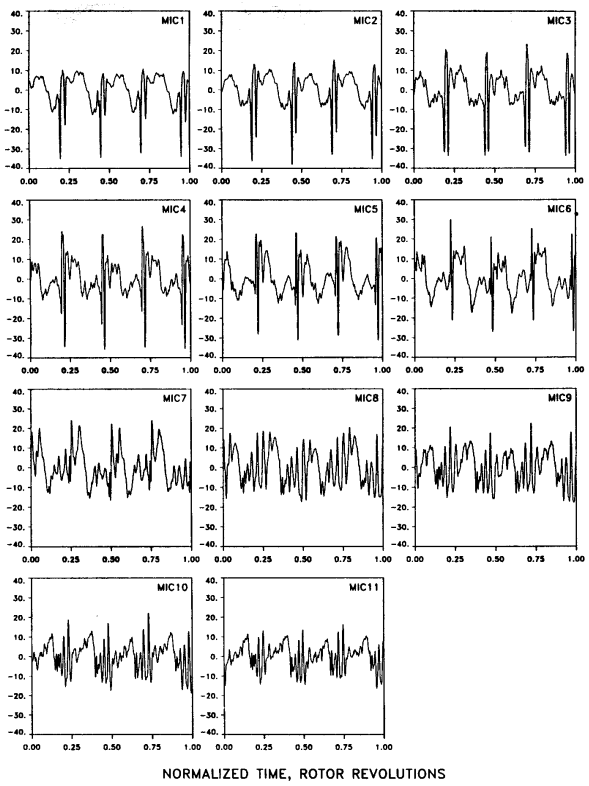

Figure A2